Journal of Structural Geology xxx (2012) 1–12

Contents lists available at SciVerse ScienceDirect

Journal of Structural Geology

journal homepage: www.elsevier.com/locate/jsg

Scaling properties of fault rocks

Hilary Dyer, David Amitrano*, Anne-Marie Boullier

ISTerre (Institut des Sciences de la Terre), UJF-CNRS, Maison des Géosciences, BP53, F-38041 Grenoble Cedex 09, France

ARTICLE INFO

Article history:
Received 28 October 2011
Received in revised form
20 June 2012
Accepted 25 June 2012
Available online xxx

Keywords:
Fault zone
Damage microstructures
Grain size distribution
Hurst coefficient

ABSTRACT

Damage structures in fault zones are well known to exhibit various scaling properties. Typically, previous studies have separated different structural descriptions of localised shear zones in order to extract their scaling properties. In this study, however, we examine simultaneously scaling properties of particles found in shear zones, described here by the particle size distribution power law exponent *D*, and scaling properties of fracture surface roughness in these same zones, described here by the Hurst exponent, *H*. We study thin sections of samples of Sidobre granite sheared in the laboratory but left unopened, thereby maintaining the original spatial context of the structures examined. Through spatial analysis we track increase of the particle power law exponent *D* with increasing local strain state. The Hurst exponent does not show a conclusive trend as a function of the strain state of the fractures for our data set. This article could lead to further work on direct spatial overlap of the two parameters directly along concentrated shear band edges.

1. Introduction

The knowledge of the damage structure within deformed rocks is of major concern for understanding the mechanical and hydraulic behaviour of the upper crust as it controls both the strength and the permeability of faults. In particular, the friction and the fluid flow during quasi-static or dynamic failure appear to be strongly influenced by the small scale structure (Candela et al., 2011), and inversely the failure process itself modifies the damage structure. Damage analysis then provides helpful information about the deformation process.

Observations at small-scale of thin sections sampled within natural faults (e.g. Boullier et al., 2004) reveal that the highly damaged zone (or shear band) is made of a granular material (i.e., gouge or cataclasite), in-filled between two rupture surfaces. The different aspects of damage in these zones (cracks, rupture surface, gouge) that result from the deformation process, can be observed either in natural conditions or at the laboratory sample scale (e.g., Keller et al., 1997; Wibberley et al., 2000). Shear deformation occurs both on the rupture surface and within the gouge layer involving friction surface erosion (e.g., Wang and Scholz, 1994) and grain fracturing (e.g., Michibayashi, 1996). The latter reduces particle size as shear progresses. Thin particles might form subshear bands as observed both at laboratory scale and at field scale (Moore et al., 1989; Menendez et al., 1996; Lin, 1999; Mair et al., 2000). Each aspect of the damage process during fracturing reveals scaling invariances (King and Sammis, 1992; Turcotte, 1992). Here we focus on surface roughness and grain size distributions as these are highly influential on the mechanical and hydraulic behaviour of faults.

1.1. Scaling properties of sheared surfaces

The rupture surfaces in heterogeneous media are characterized by a complex morphology, i.e. roughness. Statistical properties of these surfaces reveal scaling properties that make the statistical proxies (e.g. variance, standard deviation, min–max, …) depend on the scale at which they are estimated (Mandelbrot et al., 1984; Maloy et al., 1992; Cox and Wang, 1993; Power et al., 1987; Power and Durham, 1997). The concept of self-affine scaling has been proposed to model successfully the scale dependence of these parameters (Schmittbuhl et al., 1993, 1995b; Bouchaud, 1997; Lopez and Schmittbuhl, 1998). Considering the 2 D function of heights measured perpendicularly to the mean plane of the surface $h(x, y)$, the self-affine scale dependence can be expressed as (Feder, 1988):

$$h(\lambda x, \lambda y) = \lambda^{\zeta} h(x, y) \quad (1)$$

λ is a scale coefficient and ζ is the so-called roughness Hurst exponent, also known as *H*. The morphology of the surface at a given scale can be deduced from a different scale by an affine transform. The Hurst exponent has been first found to be intriguingly close to 0.8 for numerous surfaces with an apparent independency to the material properties or the loading conditions. This

* Corresponding author.
E-mail address: david.amitrano@ujf-grenoble.fr (D. Amitrano).

0191-8141/$ – see front matter © 2012 Published by Elsevier Ltd.
http://dx.doi.org/10.1016/j.jsg.2012.06.016

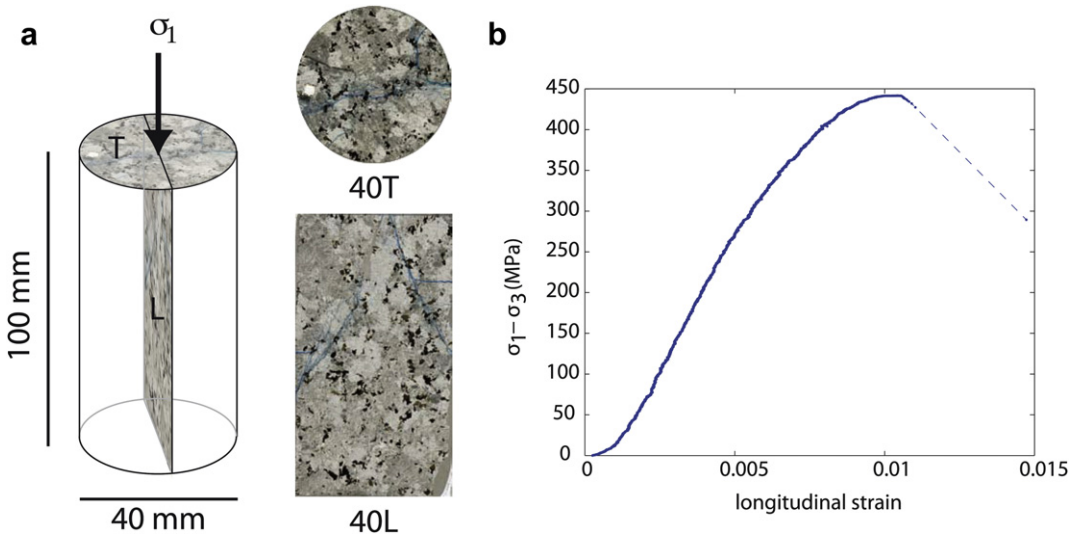

Fig. 1. a) Orientations and scans of the thin sections cut from the granite sample triaxially tested. b) Stress-strain curve of the loading test under $\sigma_3 = 40$ MPa.

leads to the early claim that the roughness exponent could be universal (Bouchaud et al., 1990). More recent observations and numerical simulations have revealed that particularly low values may be recovered for highly heterogeneous materials as sandstone (Boffa et al., 1998) or/and at very small scales (Alava et al., 2006). As these low values diverge from value of 0.8, this has been considered as an anomalous scaling. The major part of these studies is performed on surfaces obtained in the laboratory by crack opening (mode I) that corresponds to rarely observed natural conditions. The less-well documented case of the self-affine properties of shearing surfaces has been studied at the scale of laboratory sample (Amitrano and Schmittbuhl, 2002) or at the scale of natural faults (Renard et al., 2006; Candela et al., 2012; Bistacchi et al., 2011). A common observation concerning natural faults is that both the Hurst exponent and roughness amplitude are anisotropic, H being lower (nearing 0.6) in the direction of slip whereas the amplitude is larger in the direction perpendicular.

1.2. Scaling properties of gouge particles

In zones of high damage in faults, both in the laboratory and in natural conditions, the observation of scale-invariance exhibited by the distribution of rock particle sizes is well-established. Sammis et al. (1986) initially described fault gouge particle distributions from the Lopez fault as fitting a log-normal law, but this is later discarded (Sammis et al., 1987), under new sampling methods, in favour of a self-similar distribution, or power-law distribution, described parametrically by the power law exponent β of the grain-size distribution:

$$p(d) \sim d^{-\beta} \tag{2}$$

where d is a measure of grain size. β is sometimes also known as D, the fractal dimension. The results of Sammis et al. (1987) found the power law exponent describing the Lopez fault gouge produced from crystalline gneiss to be 2.60 and proposed to explain this by assuming dependence of particle fracture probability on the relative size of neighbouring particles, not on outright particle size. Under constrained conditions, homogeneous strain, and scale-independent strain, adjacent particles of the same size have the highest probability to fracture and no particular size is favoured for rupture. This 'constrained comminution' theory leads to a power-law exponent of 2.58. Subsequent studies on both experimental fault surfaces and for natural fault gouge typically show a range of different values of power-law exponents. Values equivalent to lower than 2.58 for crystalline rocks are attributed to low strain values (Marone and Scholz, 1989), with a progression to reach a value of 2.58 tracked by a simultaneous increase in strain (An and Sammis, 1994) and progression in the packing arrangement from loose to consolidated (Monzawa and Otsuki, 2003). Power-law exponents equivalent to values larger than 2.58 are typically found in localised areas of extremely high concentration of strain e.g. (Blenkinsop, 1991; Monzawa and Otsuki, 2003). These localised bands are identified to be even within the global gouge zone (Hadizadeh and Johnson, 2003; Chester et al., 2005). Explanations for this increase above 2.58 are proposed to lie in the change in conditions from fully-constrained to a small degree of freedom of motion (Sammis and King, 2007; Abe and Mair, 2005).

There appear to be limits on the applicable size ranges of the power law exponents of gouge particle size distributions. Due to observation methods used, the smallest particle sizes in initial investigations had radius measurements of the order of a few μm. More recent studies (Heilbronner and Keulen, 2006; Keulen et al., 2007) identify an abrupt reduction in power law exponent for particle sizes below a limit radius of 1–2 μm, which is proposed to be the separation size between grinding processes (larger grain size) and attrition processes (smaller grain size). A parallel is drawn with the theoretical size limit of a few μm to which various mineral and rock particles may be comminuted under compression (grinding limit, Kendall, 1978), manifested in commercial crushing operations.

In all of the studies evoked in the above, the rupture surfaces produced by shearing and the particles produced in the damage process are studied separately. Significantly, in the case of rupture surfaces in both laboratory and in field observations, observations are made after denudation (either due to the opening and cleaning of a failed sample or due to the natural erosion removing the gouge). This does not allow an examination of the potential relationship between surface roughness and gouge structure. In this paper, thin sections of granite shear zones are analysed, simultaneously for the scaling properties of the rupture surfaces, and the gouge particle size distribution. This allows a re-assembly of the

Please cite this article in press as: Dyer, H., et al., Scaling properties of fault rocks, Journal of Structural Geology (2012), http://dx.doi.org/10.1016/j.jsg.2012.06.016

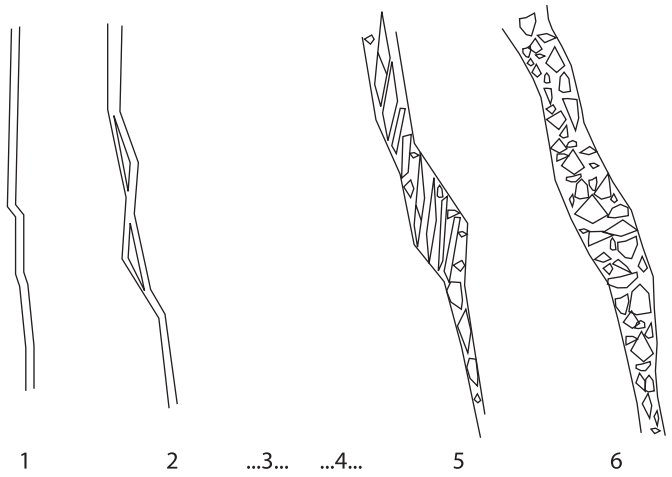

Fig. 2. Simplified classification of the different fracture types from Type 1 to Type 6.

rupture surface and the gouge structure after their separate analyses, to add information to the existing picture of the mechanisms at work in shearing damage in rock.

2. Data

2.1. Failure experiment methods

The thin sections used in the analysis are taken from a cylindrical 40 mm × 100 mm Sidobre granite sample (71% feldspar, 24,5% quartz, 4% mica, 0.5% chlorite) subject to a triaxial test at a confining pressure of 40 MPa. The complete testing apparatus is of stiffness 1×10^9 N/m. The rate of axial piston displacement is constant to the point of macrofailure at a rate of 1–2 μm/s, and the test is stopped immediately after the peak deviatoric stress is reached (Fig. 1b). Due to the low stiffness of the loading frame, the macrofailure is associated with a dynamic rupture due to elastic energy release. The final displacement distance along the developed fault is ~2 mm. The triaxial testing is identical to that described in Amitrano and Schmittbuhl (2002). After removal from the testing system, epoxy resin is injected into the sample fault. The resin is impregnated into the sample fault before the thin section is cut, under warm conditions and in a partial vacuum that disables the apparition of air bubbles. These conditions allow spreading by capillarity effect of the resin into the fractures, aided by the low viscosity of the resin and its readiness to wet surfaces it encounters. Two thin sections are then cut from the sample; the orientations of the two sections are shown in Fig. 1a. The section termed longitudinal is cut parallel to the sample cylindrical long axis, in a plane perpendicular to the emerged fault line at the sample end. When viewed parallel with the fault plane, the acute angle between the longitudinal section axis and the fault plane is ~30°. The transverse section is not discussed in this paper.

2.2. Image creation and image treatment methods

Images are made of the longitudinal thin section using Scanning Electron Microscopes (SEM), after carbon coating. A Hitachi S-2500 SEM with a W filament is used at two different diaphragm sizes. All images are Back-Scattered Electron images. A range of image magnifications are used; these are given in the Appendix and explained in the following results sections. The injected resin has a different atomic mass to all surrounding minerals and provides a clear distinction of fracture lines in the digital images produced by the SEMs. In order to relate the different fractures to the *H* and *D* parameters and to the advance of the fracturing processes, the fractures were qualitatively classified into six types by intuitive increasing order of strain state (Fig. 2) using the raw SEM images.

The following is a brief overview of the image treatment methods used. Complete details are given in the Supplementary Information (SI) section.

A Multi-stage Recursive Median filter (Bolon and Raji, 1991) is applied to each image to remove noise. This filter has been shown to be advantageous in the preservation of line geometry within the image, whilst still effectively removing noise (see SI). The images are represented in indexed format (a colour-map of pixel labels of integers from 0 to 255) and a simple threshold is selected and applied to the images to create a binary image of areas of resin (fractures) and areas of the sample structure itself. The simple threshold segmentation technique is sufficient to obtain complete segmentation of the sample structure from the interstitial fractures, thus delineating both the fracture geometry and the particle shapes and sizes. In all cases the resulting segmented images are then processed using the Matlab Image Processing toolbox to obtain the geometrical characteristics of the image contents and thus of the thin section structures. The locations of the images from the thin section were chosen at random and a pre-selection of these for use in the analysis was made based on the longest and clearest fractures available.

2.3. Analysis methods

Fracture edges within the images are selected for analysis by approaching the image from one side and analysing fractures met in the path of this scanning direction. In the case of branched fractures, the principle of selection of fracture paths is to start from the edge of the image, or an area of intact rock within the image, and to move towards a fractured area. On encountering a fracture, its height profile is extracted by recording the relative locations of the pixels which represent the fracture front. A preference is given to the longest fractures in the images as this presents an advantage for statistical stability in the roughness analysis. Fractures which have natural high connectivity after the image treatment process are preferred. After the first fracture is encountered, several other possible fracture paths for the same fracture behaviour are also extracted. This leads to a non-deterministic analysis of the fractures in the images selected, in areas where a single macrofracture has not developed. It is found repetitively that different fracture paths at the same site yield insignificant variations in *H*-values from the perceived main fracture path, which removes the question of a single *H*-value falsely representing a certain characteristic fracture type. Each fracture is described by its variation in height, in the direction perpendicular to its general direction of progression. Rotation of the images is carried out where necessary in order to minimise the overall trend occurring in the fractures analysed. These discretised profiles of the fracture topography then permit direct analysis of the *H*-values. Details of the fractures analysed are found in Table SI2 of the SI section. Seven different analysis methods are applied; maximum–minimum bandwidth, root-mean-square bandwidth, root-mean-square of the height difference, mean of the height difference, two point correlation function, Fourier spectrum, and multi-return probability. Except the Fourier spectrum method, all these methods are based on the calculation of a statistical estimator as a function of the length over which it is estimated. That can be the root-mean-square of the height within a segment extremity (rms1) or of the height difference (rms2); the mean value of height difference (dif h); the point to point correlation (cor); the min–max difference (mmd); the probability of crossing a horizontal line (multi-return probability, mrp). As an

Please cite this article in press as: Dyer, H., et al., Scaling properties of fault rocks, Journal of Structural Geology (2012), http://dx.doi.org/10.1016/j.jsg.2012.06.016

example of Hurst exponent calculation, for the root-mean-square correlation method over a profile in x–z space, the standard deviation value of the height differences ($h(x+\Delta x) - h(x)$) of all pairs of points separated by distance Δx is calculated, the separation distance Δx is varied between 1 and the length of the profile and a graph in log–log scale of these separation distances against the corresponding root-mean-square height differences produces a straight line with a slope equal to the Hurst exponent. Demonstrating the typical graph form produced, the actual results obtained with the rms2 method are then all illustrated in Fig. 3. For more detailed method descriptions, we refer to Schmittbuhl et al. (1995a), Candela et al. (2009) and Bouchaud et al. (1993). Following Schmittbuhl et al. (1995a) the objective in this paper of using several different analysis methods is to exploit the overall average H-value as the Hurst exponent for each profile. This is because each method contains intrinsic biases in the measurements that vary with profile length and Hurst exponent value. Although the Fourier spectrum method alone has been tested to be the most accurate method of Hurst exponent extraction for surfaces (Candela et al., 2009), when considering a single profile, this method loses superiority due to the instability of the higher end of the spectrum. This defect could be reduced by applying an apodisation function, ie. a progressive reduction of the amplitude at the beginning and ending of the signal, since this would avoid sudden changes in the signal that introduces high frequency. We estimated the reliability of the methods we used by calculating the H exponent on synthetic profiles of controlled H (see SI). The systematic biases in H estimation were estimated and taken into account for the H estimation made for the profiles extracted from images. The results of mrp and mmd methods were not taken into account as these two methods were characterised by very important biases.

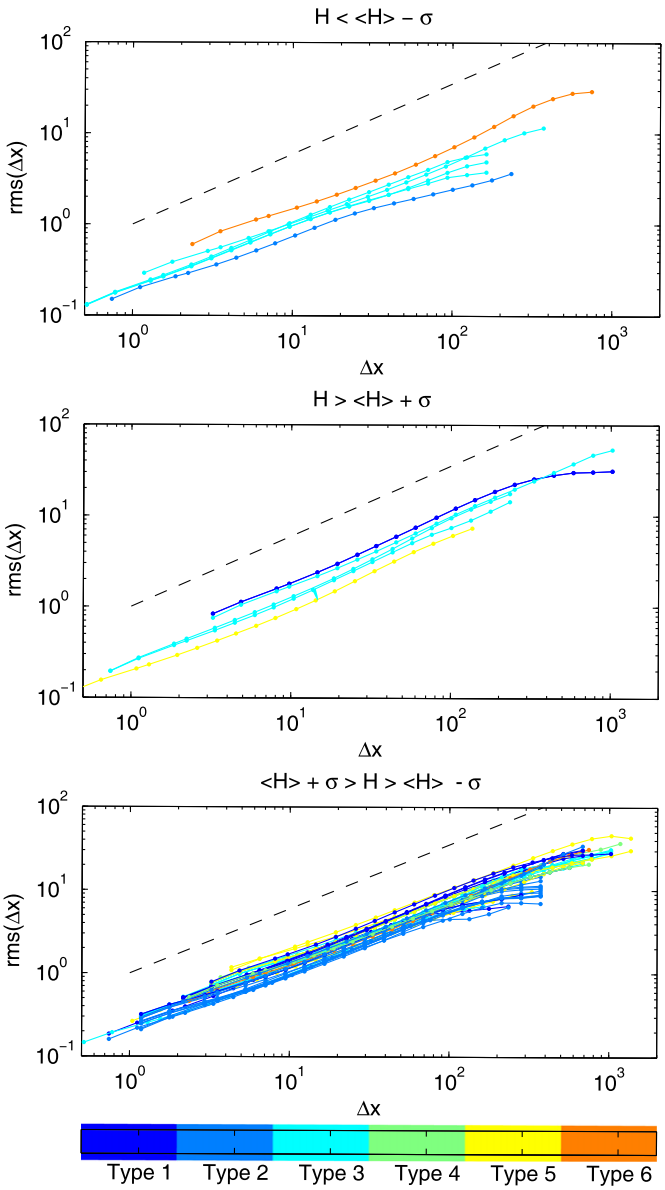

Fig. 3. Graphs representing the analysis of the Hurst exponent by the rms2 method. The fractures are divided into three groups; one (top) for those of Hurst exponent above one σ from the mean of the set, a second (middle) for those of Hurst exponent below one σ from the set mean, and a third (bottom) for those between one σ above and below the set mean. The dotted lines are given as guidelines and correspond to the mean value $H = 0.78$.

In the case of the gouge particles, after identification of individual particles within the gouge zones, the particle areas are calculated using Matlab functions. This measurement is retained in order to bypass the use of formulae which would assume spherical particles, which is clearly not the case in many of the shear zones analysed. The distributions are described using a power law exponent, relevant to the 2-D nature of the images under analysis, and referred to as D_{2D}. It should be noted that particles cut by the edges of the images are removed before particle size analysis as these would present incorrect size data (known as the 'sampling effect', Sammis et al. (1987)). Example images showing the extracted fracture fronts and the identified grains are found in Fig. SI4 of the SI section.

3. Results and discussion

3.1. Fracture surface roughness

Using the Hurst exponents of the retained methods (see SI), the profiles are rank ordered according to mean Hurst exponent (Fig. 4a). We then calculate for the entire set of mean Hurst exponents, the overall mean Hurst exponent value and the value of one and two standard deviations from the mean (Fig. 4b). The value of the set mean Hurst exponent is 0.78 with standard deviation of 0.07. Using the statistical reasoning that if our data is contained within 2 standard deviations either side of the mean value, the variations within the set can be considered insignificant with 95% confidence, we find there is strong argument to accept the mean Hurst value as representative of the entire set and to consider the variations within the set negligible. We represent all graphs in Fig. 3 which are extracted from the statistical analysis using the rms method to find the Hurst exponent of the fractures. We separate the graphs into groups depending on their situation with respect to the statistical parameters (mean and standard deviation) of the entire set. We notice no particular characteristics corresponding to any of the grouped graphs and therefore no particular characteristics of the outliers of the limit for acceptance with 95% confidence of the insignificance of the variations in the set. Noting that the orientation of the longitudinal thin section is such that the direction of shear motion along the fracture plane is parallel to the macroscopic fracture direction on the section, and that recent work (Candela et al., 2012) has established a reduction in Hurst exponent to ~0.65 on many examples of fault surfaces, we may have expected a concentration of values of $H \sim 0.65$ from all fracture profiles in this thin section. We notice that our mean value is higher than this documented value.

Neglecting the variations in the set implies that all fractures can be grouped together in a scaling description but does not explain why this is the case. To look more closely at the structural

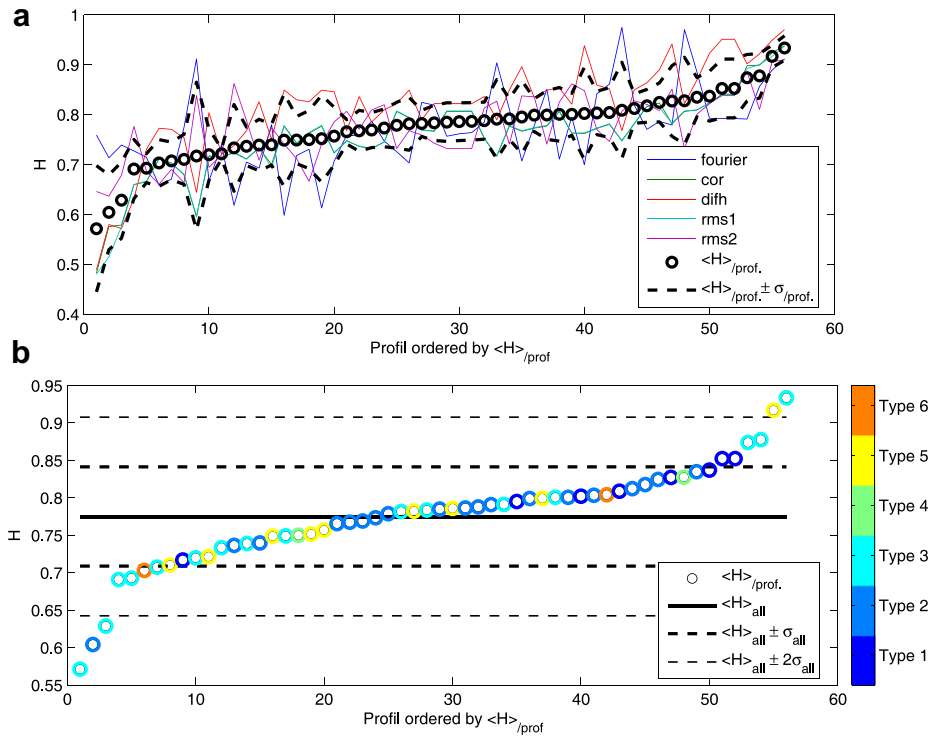

Fig. 4. All retained methods of calculation of the Hurst exponent represented individually, showing sufficient concordance of the Hurst exponent variation depending on method. a) The fractures are rank ordered by the mean Hurst exponent, which is then superimposed on the different methods, along with the standard deviations. b) The mean of the entire set of mean Hurst exponents, and one and two standard deviations either side of this are plotted with the individual mean Hurst exponents.

differences in the set of profiles, they are then sorted into categories attempting to group together different stages in fracture development following Fig. 2. The categories follow stages of strain observed by eye from initial Mode I fracture creation (Type 1) to shear band of separated particles (Type 6); this is illustrated in Fig. 2. Each step in the classification corresponds to the context of the fracture in terms of particle creation and fracture branching that are signs of shear behaviour along the fracture. Using Figs. 2 and 4, we make the following notable observations:

(1) In general a high Hurst exponent of 0.8–0.85 for fractures of Type 1.
(2) An apparent slight decrease in the Hurst exponent for fractures of Types 2 and 3, compared to Type 1. This trend becomes unclear for Types 4, 5 and 6.

Referring to notable observation (1) as just defined, Mode 1 fractures have been found to produce fracture surfaces of $H \sim 0{,}8$ for many different materials, including granite (Schmittbuhl et al., 1994). Referring to notable observation (2), the apparent decrease may be explained by observations made in Amitrano and Schmittbuhl (2002) who use the same samples but with different methods of analysing H, that at macroscopic scale the Hurst exponent of shear zone edges decreases slightly with accumulation of shearing displacement in samples of the same granite as used in this study. However, the discontinuity of this decreasing trend for fracture types 4, 5 and 6 means it is unreliable to conclude that we are really observing the effect of increased slip on the fractures. We consider a second possible explanation for the variation in Hurst exponent within the set to be the acute angle between the direction of the fracture formed and σ_1. Bistacchi et al. (2011) found fault planes at orientations of low angle to the principal stress direction are associated with high Hurst exponents and fault planes orientated at high angles (nearing 90°) to the principal stress are associated with lower Hurst exponents. This would indicate a correspondence between the effect of slip on a fault, which is a function of the self-affine regime. However in this study, as shown in Fig. 5, there is no clear correlation between the acute angle of the fracture to σ_1 and the Hurst exponent. This may be due to the effects of local stress fields producing different local orientations of the principal stresses. After considering these possible explanations for the Hurst exponent variation we return to our original conclusion that although there appears to be a weak trend of decreasing

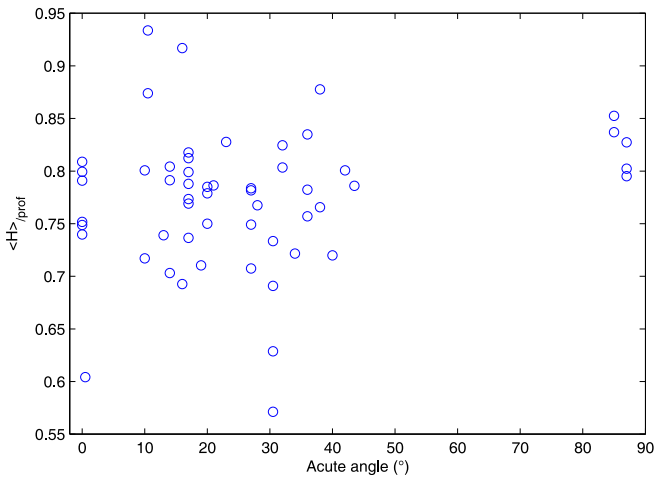

Fig. 5. Mean Hurst exponents of individual fractures as a function of the acute angle of the fracture orientation to the direction of σ_1.

Please cite this article in press as: Dyer, H., et al., Scaling properties of fault rocks, Journal of Structural Geology (2012), http://dx.doi.org/10.1016/j.jsg.2012.06.016

Table 1
Values of the power law exponent of particle size distributions for the five shear zones A to E (illustrated in Fig. 6).

Image	Pixel (μm)	$D_{2D<}$		$D_{2D>}$		d_k (μm)[a]
A	0.76	–	–	1.83	±0.03	4
B	0.43	1.26	±0.02	2.28	±0.04	4
C	1.18	–	–	1.68	±0.05	7
D	1.18	1.03	±0.02	1.53	±0.04	9
E	0.13	1.14	±0.02	1.63	±0.01	12

[a] Denotes the crossover grain diameter.

Hurst exponent with increasing strain state of the fracture, this trend remains incomplete and we describe the scaling properties of the roughness of the set of fractures by a single mean value with variations of little significance.

3.2. Particle size distributions

We look now at scale invariance in particle size distributions in formed fault zones in the thin section. Initially, several different shear zones are examined within the longitudinal thin section; named A, B, C, D, and E. The SEM images, after segmentation and grain identification, and the cumulative particle size distributions for these five shear areas are shown in Fig. 6, and the corresponding D_{2D} values are shown in Table 1. The particle size distributions, particularly for images B and E, show an apparent change in slope suggesting a reduced power law exponent for smaller particle sizes. However, simultaneously, at this lower end of the particle size distribution, a degree of flattening is expected due to limitations on particle detection at each chosen image resolution (see later in this

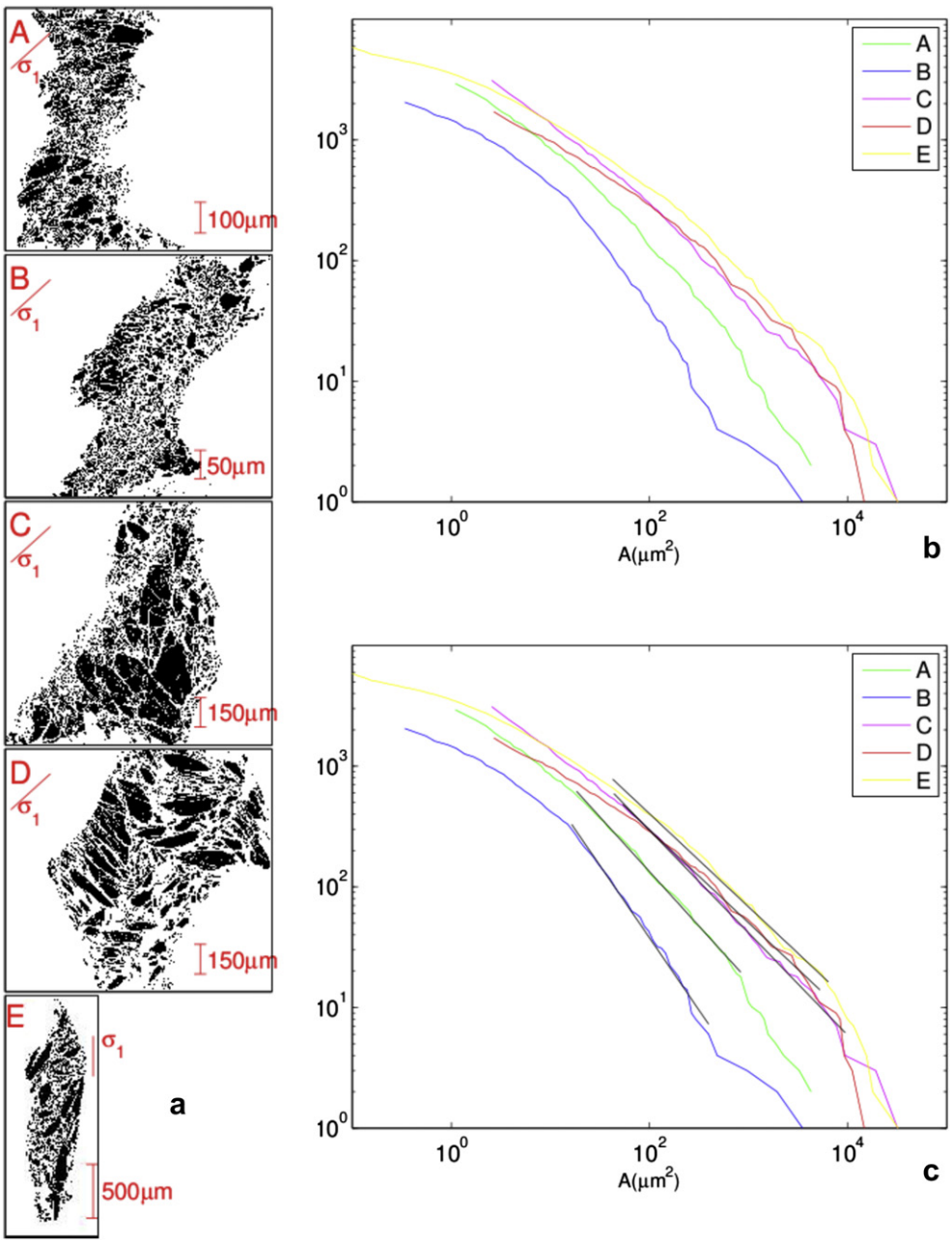

Fig. 6. Initial five shear zones A–E from the longitudinal thin section. a) segmented SEM images of the shear zones. b) corresponding particle size distributions. c) the same particle size distributions are shown with the power law fit superimposed, for exponents $D_{2D>}$.

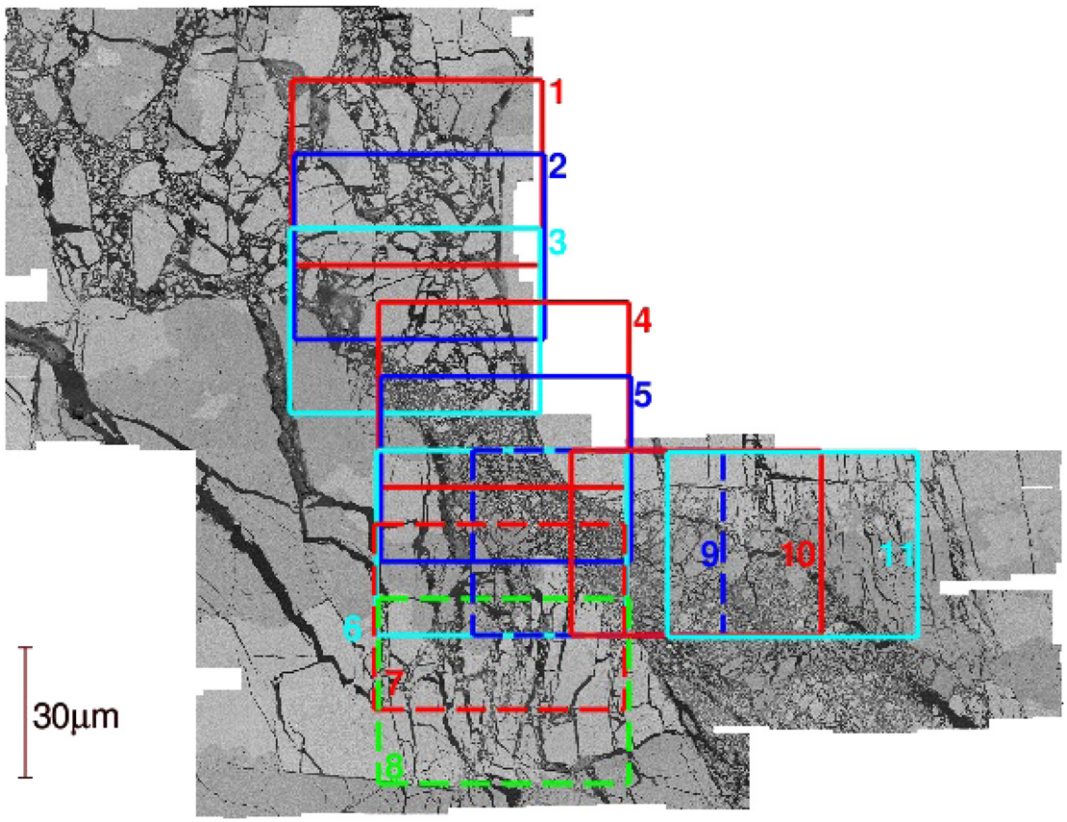

Fig. 7. Mosaic constructed from higher-resolution images of an extended area of image B from Fig. 6. Selected areas for particle size distribution analysis are outlined and labelled. The line types are selected only for clearer differentiation between rectangles and have no further significance. The direction of σ_1 is parallel to the vertical edge of the image.

section). It is found that the best-fitting series of power law exponents for these power law distributions consists of two different exponents for images B and E, (one for higher grain sizes and the other for lower grain sizes), but that for images A, C and D it is difficult to clearly define a separate power law for lower grain sizes. The power laws reported in Table 1 have been calculated using a maximum and minimum ending point at the larger particle size end of the relevant range of the distribution (one or two described areas), and varying the starting point for both possible ending values. The lowest standard deviation of the errors for the power law fit for all combinations allows us to determine a lower and upper bound, and therefore an error bar. The diameter at which there is an estimated cross-over between the two different exponents is denoted d_k, power-law exponents referring to particle sizes greater than this are denoted $D_{2D>}$ and power-law exponents referring to particle sizes below d_k are denoted $D_{2D<}$. Considering firstly the values of $D_{2D>}$, a first observation is the existence of lower power law exponents, at $D_{2D>} = 1.53–1.68$, a slightly higher value for image A, and a largely higher value for image B of $D_{2D>} = 2.28 \pm 0.04$. In this study the first series corresponds to zones where grains are highly angular, yet separated from their original cracked formation, and the different largely higher value corresponds to a zone where the particles have less angular shapes, and are more closely packed. At this stage no spatial variation in D is considered because the local shear zone in the image is considered in its entirety. However, considering only the D-values themselves, the value range ~1.53–1.68 corresponds loosely within error bars to the 'constrained comminution' model of Sammis et al. (1987) detailed in Section 1. The higher value $D_{2D>}$ for image B is similar to high values of D which are proposed elsewhere to be explained by conditions of high strain concentration (Monzawa and Otsuki, 2003) and are associated with the addition of a local small degree of freedom of motion to the shear zone which leads on a theoretical basis (Sammis and King, 2007) to a higher particle size distribution power law exponent, also produced from modelling (Abe and Mair, 2005). The observed differences of D-values for the images A to E are also concordant with those made by Keulen et al. (2007) and Heilbronner and Keulen (2006) for cracked grains ($D = 1.6$) and developed gouge ($D = 2.2$) referring to grain sizes above $d_k \sim 2$ μm. The range over which these exponents are fitted varies due to the slightly different magnifications of the different images. For images A and B the power law extends over only one order of magnitude whilst for the others three images we are approaching 2 orders of magnitude. There is a common range for all five images of the scales at which these power laws apply around the area value 100 μm^2, and the relatively similar values of d_k that are found attest to a feasible comparison between the different images.

Considering now, for the five shear zones in this study, the values of $D_{2D<}$, the value of approximately 1 which is common to the images for which this parameter has been identified is again also found by Keulen et al. (2007) and Heilbronner and Keulen (2006). Finally, considering the grain size cross-over diameter, d_k, between the two power-law exponent regimes, the value of d_k for this study is estimated as slightly higher than that in previous literature (Heilbronner and Keulen, 2006; Keulen et al., 2007). This comparison is complicated by the consideration in these two references of the particles as spherical in order to define the particles in 2-D using the description of a circle. In this study the particles are also treated as spherical to calculate d_k but this is not an ideal assumption since the particles are clearly not spherical. A second reason for the difference in values of d_k may arise from the identification of the change in power law initially by eye and then

Please cite this article in press as: Dyer, H., et al., Scaling properties of fault rocks, Journal of Structural Geology (2012), http://dx.doi.org/10.1016/j.jsg.2012.06.016

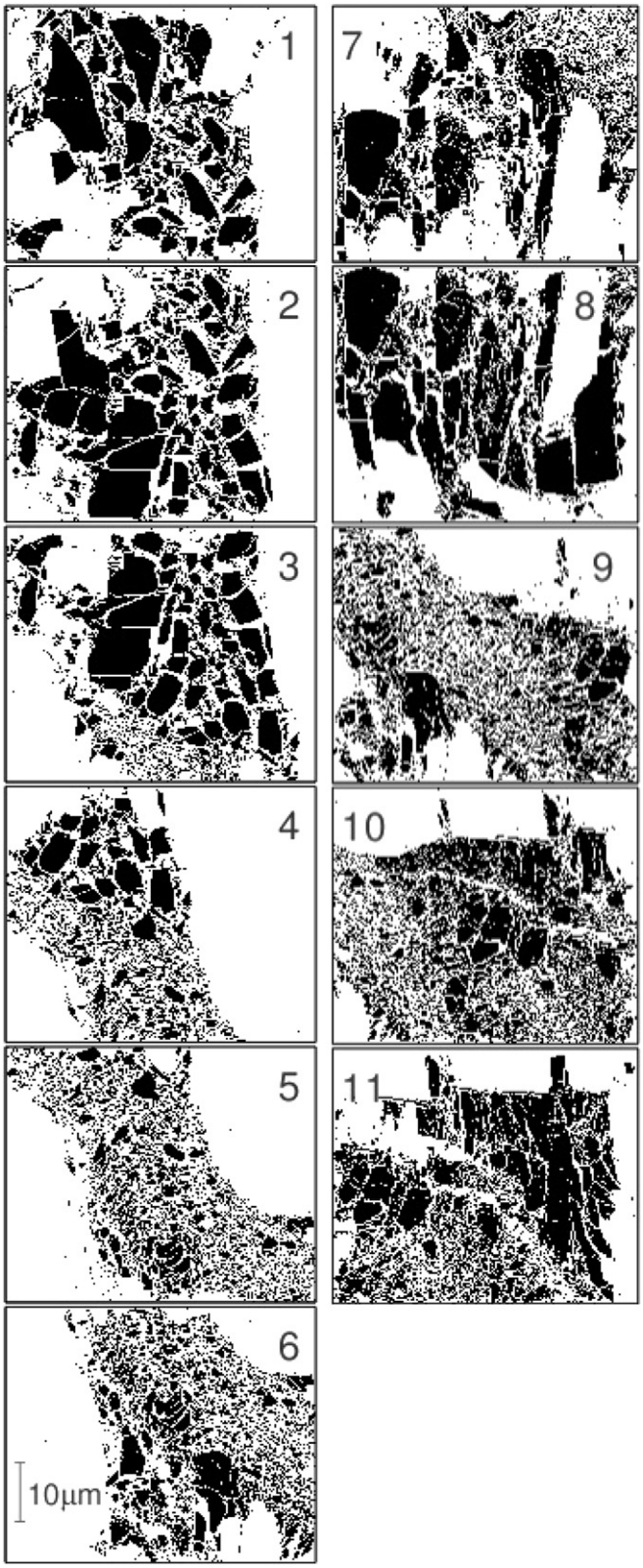

Fig. 8. Segmented SEM images of the rectangles selected in Fig. 7.

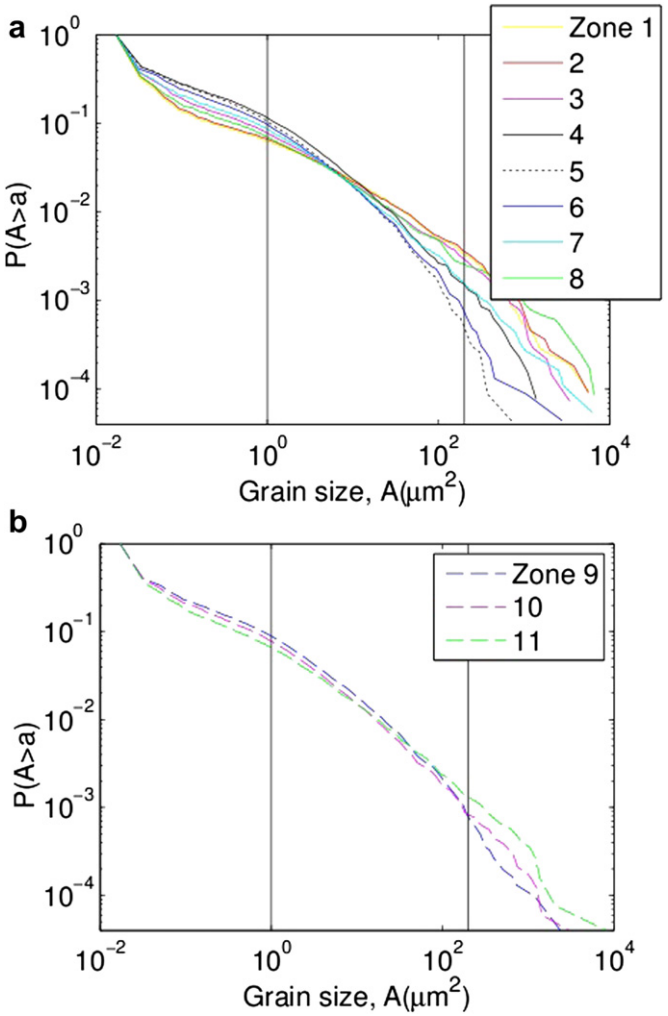

Fig. 9. Particle size distributions of the segmentation of Fig. 8. Two different graph spaces are used for clarity.

by finding the power law fit with the lowest errors. This process means the determination of the exact point of change between the two power laws still retains a certain error due to the curved nature of some of the distributions. The physical explanation offered for the change in power-law exponent for different particle scale ranges for granitoid rocks is that of transferring from processes of grinding or compressional fracturing (large grain sizes) to those involving attrition (small grain sizes). This difference in values is also repeated in high-velocity situations by Stünitz et al. (2010). The particle size at the point of power-law exponent change is generally explained by a 'grinding limit' at which particles cannot be reduced further in size by fracturing. We note that for images A and B the reported d_k value in Table 1 is lower than for the other images. This corresponds to the raised $D_{2D>}$ value for these images, which in turn corresponds to the increased strain state for these local shear zones, in particular image B. To continue the discussion, Kendall (1978) cites variations on the order of a few micrometres in the size value of the transition from fracturing to grinding for different materials and minerals, and Steier and Schönert (1972, in Prasher, 1987) cites the grinding limit of quartz to be 0.9 μm. Since the grinding limit value for quartz is apparently lower than other minerals, the higher quartz content (35%) of the granitoid rocks used in Heilbronner and Keulen (2006) and Keulen et al. (2007) may contribute to produce a lower grinding limit value than for the Sidobre granite (24.5%) samples we use in this study.

We will now consider only the values of $D_{2D>}$ in the context of a spatial analysis within a specific part of a local shear zone in order to further investigate the variation in this particular parameter. A series of higher-resolution images constituting a mosaic of an

Please cite this article in press as: Dyer, H., et al., Scaling properties of fault rocks, Journal of Structural Geology (2012), http://dx.doi.org/10.1016/j.jsg.2012.06.016

Table 2
Values of the power law exponent of particle size distributions for the frames defined in Fig. 7.

Frame	$D_{2D>}$[a]
1	−1.14
2	−1.13
3	−1.26
4	−1.70
5	−1.96
6	−1.80
7	−1.53
8	−1.27
9	−1.72
10	−1.70
11	−1.48

[a] Error bars are all inferior to ± 0.02.

extended area of image B from Fig. 6 allows a spatial analysis of the variation in particle size distributions. A mosaic image construction allows the image magnification to remain high whilst the number of particles in the size distribution is kept as large as possible and the large particles are less affected by the image edges cutting through them. The mosaic image illustrating the selected frames is found in Fig. 7, and the corresponding framed areas are represented in Fig. 8 as segmented SEM images and Fig. 9 as cumulative particle size distributions. Table 2 contains the *D*-values for each frame. The range of particle diameters over which the power law exponent is calculated is constant for all windows and is marked on Fig. 9, and the error bars for each exponent are calculated using the standard deviation of the errors of the power law fit. Overall, there is a trend in the particle size distribution power-law exponents which corresponds well to identifiable differences in the appearance of the shear zone section in each framed zone. A first group is frames 1, 2, 3, and 8, which exhibit low $D_{2D>}$ values of ~1.1–1.2 in areas of a dense network of cracks which are situated at some distance from the concentrated gouge zones. Frames 5 and 6, corresponding to highly-comminuted gouge zones, yield the highest $D_{2D>}$ values, of ~1.8–2.0. Between these two groups, other frames of $D_{2D>}$ in the range ~1.45–1.66 are in areas of abrupt cross-over between two different comminution levels, or frame zones which are spatially situated between highly-comminuted gouge and in-situ cracked grains. The low *D*-values in the first group have also been reported by Marone and Scholz (1989) for experiments under low strain values said to be insufficient to produce 'constrained comminution' conditions. The progression of the $D_{2D>}$ value is significantly similar to an increase in *D*-value to an eventual $D = 2.6$ associated with increasing strain (An and Sammis, 1994), which corresponds to the theoretical value of 2.58 proposed by Sammis et al. (1987). The present spatial analysis, illustrates that the local strain state at different sections of a developing shear zone is reflected in the local particle size distribution power law exponent. In in-situ faults, this variation in degree of development of the comminution process in different zones of a fault is a common observation (Hadizadeh and Johnson, 2003; Chester et al., 2005) and has previously been quantified by Blenkinsop (1991).

In general, the best correspondence to a power law distribution is found for those windows selected well within an apparently easily-distinguished gouge particle type. Windows overlapping or containing more than one particle type tend to exhibit far greater curvature of the power law (eg. Fig. 8, windows 4 and 11). This suggests that a curved shape on the graph may be a cross-over of two different distributions without a clearly defined size of particle separating the two.

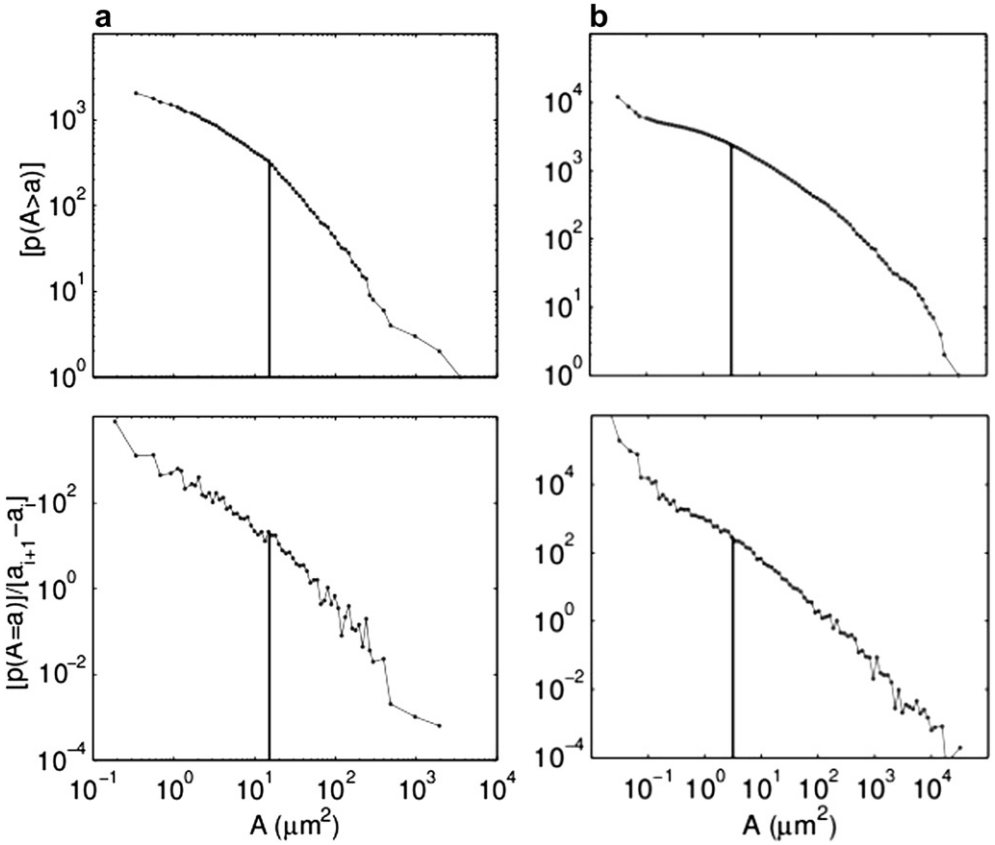

Fig. 10. Reduced particle size distributions for images B and E from Fig. 6. Each column consists of two distribution types, for each of the two grain geometry measurements; Row 1, the original cumulative distribution (cdf): Row 2, the reduced probability distribution (pdf/classwidth). The proposed crossover grain size is indicated. a) Image B. b) Image E.

We will now further develop considerations of the particle size distributions in the size range below the cross-over grain diameter d_k. In the case of the original five images A to E a change in slope has been identified on certain cumulative probability distributions. This is clearest to observe by eye in Fig. 6 for image B, but appears still present also in image E. We acknowledged earlier in this section that a power law flattening is expected at the lower end of the size ranges due to the imaging techniques used. In order to verify that the flattening observed is not induced by sampling effect, the reduced discrete probability distribution (probability density function, pdf) is presented in Fig. 10a and b for images B and E, respectively. This takes into account both the number of particles and the bin width; by "reduced" we refer to the division of the value of the probability distribution corresponding to each class by the width of that class. If the gradient of the slope of the pdf is positive below a supposed change in slope, the influence of the sampling effects would have been judged dominant, whereas if the gradient remains negative, the change in slope value can be judged valid. The reduced distribution slopes in these cases maintain the negative gradient at grain sizes below the change in slope which indicates that the change in slope initially seen in the cumulative probability distributions in Fig. 6 is not due to sampling effects.

3.3. Particle orientation–size relations

Elongated particle shapes are particularly observed on images D and E from the initial series of images in Fig. 6. As seen in Table 1 and Section 3.2, the power low exponents $D_{2D>}$of these images are in the range typical of a 'constrained comminution' situation (Image D) or have a level of comminution just prior to this 'constrained' situation (Image E). Due to the initial elongated shape of the particles, considerations of the particle long-axis orientations in relation to the size of the particle offer more information on the mechanisms at work at this stage of the comminution process in these particular shear bands. Scatter plots in Fig. 11 plot, for each particle; long-axis length, short-axis length, and ratio min–max, as a function of the clockwise acute angle of orientation of the particle long-axis with respect to σ_1. For both of the shear zones considered, the smaller particles in the distributions show no particular orientations, whether they are described by their maximum axis length, minimum axis length, or axis ratio max/min. As the axis length ratio increases certain long-axis orientations become dominant. For Image E (Fig. 11b), above a length ratio of 4, the dominant particle orientation is positive, and the particles with the largest ratios are those with small positive angles to σ_1. Interpreting this in terms of the mechanism, large particles are initially associated with high axis length ratios and are at low orientations to σ_1, They are mainly created by mode I cracks. Then as particles are fractured, reducing both their size and axis length ratios, they are rotated by the shearing action at work in the shear zone to reach higher orientations to σ_1. On further fracturing, the particle size ratio and the different orientations become indistinguishable. For Image D (Fig. 11a), in terms of the major axis length, some mid-size particles are clustered around a particle orientation at a near right-angle to σ_1, whereas the longest major axis lengths are spread over a range of orientations from 0° to −90° from σ_1, with a particular

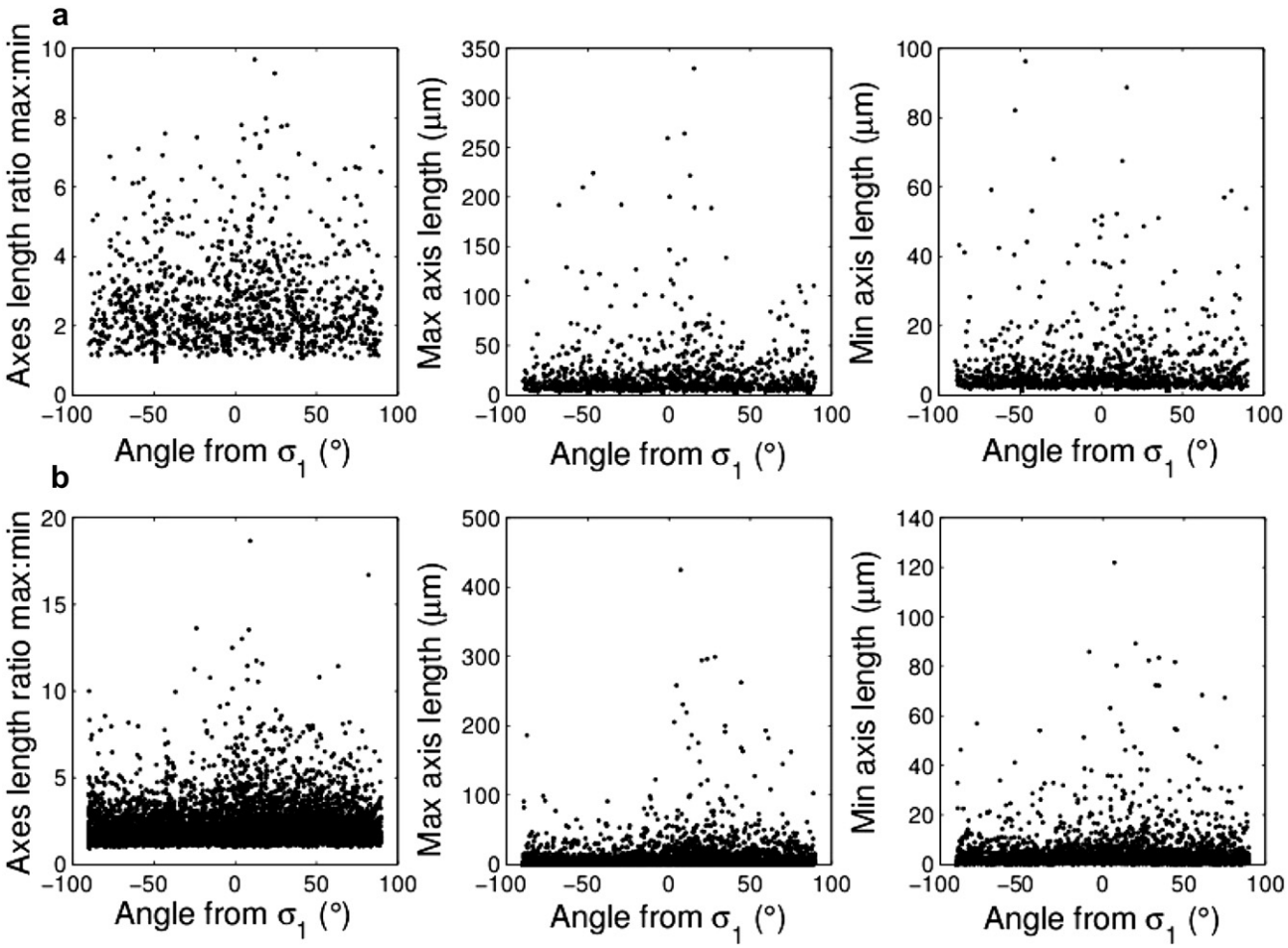

Fig. 11. Relations in particle orientation to particle size for images D and E from Fig. 6. a) Image D, b) Image E.

Table 3
Relationship $L_{min} \sim L_{max}^{p}$ between the minimum axis lengths and maximum axis lengths of the particles in shear zones corresponding to images A–E in Fig. 6.

Image	p[a]
A	0.86
B	0.88
C	0.84
D	0.78
E	0.90

[a] Error bars are all inferior to ±0.02.

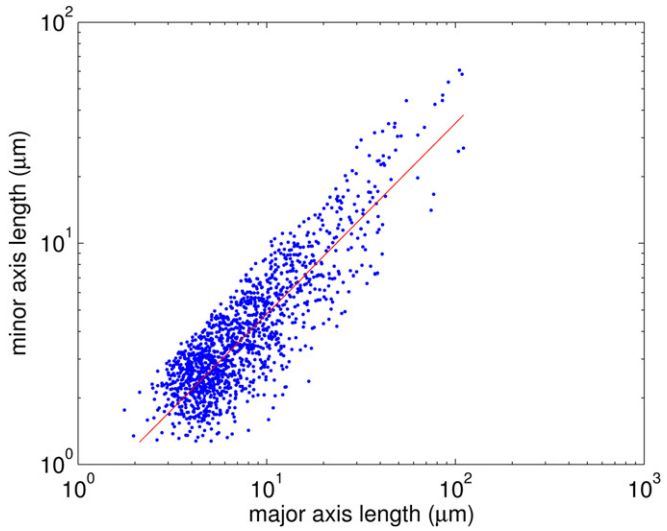

Fig. 12. Relation between the minimum axis and maximum axis lengths of the particles in the image A illustrated in Fig. 6. This figure serves as an example of the relation followed by the particles in all five images A–E.

concentration at low angles to σ_1. The axis length ratio is less indicative of the orientations for this shear zone than for Image E, but it follows the same trends as the major axis lengths. The observations in this second case again suggest that particles initially fractured by mode I cracks from the walls of the shear zone are modified from their initial sizes by simultaneous fracturing and rotation provoked by the shearing action, until reaching a particle geometry common to the full spectrum of orientations. These observations are in addition to the scale invariance considerations made on particle size distributions.

Finally, we have also considered a power law relation between the particle maximum axis lengths and minimum axis lengths for the five shear zones A–E represented in Fig. 6, in the form $L_{min} \sim L_{max}^{p}$. Tabulated results of this are found in Table 3, and an example illustration of the relation for Image A is found in Fig. 12. The values of the exponent p lower than 1 attest that particles lose their length faster than their width during the fracturing process. This is an expected result given the above observations of fracture of long particles as they are drawn into the shear zone from the edges and rotated. A simple erosion process, in which the particles result from the intersection of two self affine surfaces, lead to consider $p = H$. Such a model could satisfactorily apply for zone D but not for the others as it does not take into account the comminution process.

4. Conclusions

In this study we examine scale invariance present in the structures of shear faults in thin sections of granite, immediately post fault formation, and in the case of unopened samples. Unopened samples allow us to examine different damage structures present in the fault zone, in an in-situ context, and subsequently to re-assemble these different observations of scale invariance for a fuller description of the scale-invariant processes at work. This is an initial article on the topic of scale-invariance in fault rocks involving the simultaneous analysis of two different descriptions of fault structures.

The power law exponent of particle size distributions of fractured areas in the vicinity of faults undergoes a progressive increase in value as the particles are sampled in areas progressively approaching gouge zones of high comminution in developed shear zones. Additionally, the fracture surface roughness, described by the Hurst exponent, is looked at in fractures from a large range of locations within the thin section. No continuous general progression is found between the Hurst exponent and the strain state of each fracture as can be judged by its appearance but a slight trend is observed of reducing Hurst exponent for a change from Mode I to low concentrated strain. A better description of the Hurst exponents is found to be a mean value of 0.78 ± 0.07 with a rejection at 95% confidence of the variations in the set for this description. At this stage a direct relation between these two descriptive parameters, the particle size power law exponent and the Hurst exponent, is not definitive for the scales observed in this study. Further work could look more closely at quantifying the slip component on fractures directly at the shear zone edges, and simultaneously the particle size distributions in gouge areas directly adjacent to these specific shear zone edges, with a view to defining an empirical relation directly relating the scaling parameters of gouge particle sizes and fracture roughness in the case of fault zone damage processes.

Acknowledgements

We are grateful, to Christophe Nevado (Geosciences Montpellier) for high quality polished thin sections, to Nathaniel Findling (ISTerre, Grenoble) and Frédéric Charlot (CMTC, Grenoble) for technical help and advice when using SEM, to Jean-Robert Grasso (ISTerre Grenoble) for helpful discussions, to an anonymous reviewer and to Stéphane Santucci for his careful review and suggestions that have contributed to widely enhance the manuscript. We also gratefully acknowledge contributions from TRIGS European programme.

Appendix A. Supplementary material

Supplementary data associated with this article can be found, in the online version, at http://dx.doi.org/10.1016/j.jsg.2012.06.016.

References

Abe, S., Mair, K., 2005. Grain fracture in 3D numerical simulations of granular shear. Geophysical Research Letters 32 (3), L05305.
Alava, M., Nukala, P., Zapperi, S., 2006. Morphology of two-dimensional fracture surfaces. Journal of Statistical Mechanics: Theory and Experiment, L10002.
Amitrano, D., Schmittbuhl, J., 2002. Fracture roughness and gouge distribution of a granite shear band. Journal of Geophysical Research 107 (B12), 2375–2390.
An, L.-J., Sammis, C.G., 1994. Particle size distribution of cataclastic fault materials from Southern California: a 3-D study. Pure and Applied Geophysics 143 (1/2/3), 203–227.
Bistacchi, A., Griffith, W.A., Smith, S.A.F., Di Toro, G., Jones, R., Nielsen, S., 2011. Fault roughness at seismogenic depths from LiDAR and photogrammetric analysis. Pure and Applied Geophysics. http://dx.doi.org/10.1007/s00024-011-0301-7.
Blenkinsop, T.G., 1991. Cataclasis and processes of particle size reduction. Pure and Applied Geophysics 136, 60–86.
Boffa, J.M., Allain, C., Hulin, J.P., 1998. Experimental analysis of fracture rugosity in granular and compact rocks. European Physical Journal Applied Physics 2, 281–289.

Bolon, P., Raji, A., 1991. Filtrage médian récursif multi-étage. Etude des propriétés statistiques et morphologiques. In: Treizième colloque GRETSI, Juan-les-Pins, France, 1005–1008.
Bouchaud, E., 1997. Scaling properties of cracks. Journal of Physics: Condensed Matter 9, 4319–4344.
Bouchaud, E., Lapasset, G., Planès, J., 1990. Fractal dimension of fractured surfaces: a universal value? Europhysics Letters 13, 73–79.
Bouchaud, E., Lapasset, G., Planès, J., Naveos, S., 1993. Statistics of branched fracture surfaces. Physics Review B-Condensed Matter B48, 2917–2928.
Boullier, A.M., Fujimoto, K., Ito, H., Ohtani, T., Keulen, N., Fabbri, O., Amitrano, D., Dubois, M., Pezard, P., 2004. Structural evolution of the Nojima fault (Awaji Island, Japan) revisited from the GSJ drill hole at Hirabayashi. Earth Planets and Space 56, 1233–1240.
Candela, T., Renard, F., Bouchon, M., Brouste, A., Marsan, D., Schmittbuhl, J., Voisin, C., 2009. Characterization of fault roughness at various scales: implications of three dimensional high resolution topography measurements. Pure and Applied Geophysics 166, 1817–1851.
Candela, T., Renard, F., Bouchon, M., Schmittbuhl, J., Brodsky, E., 2011. Stress drop during earthquakes: effect of fault roughness scaling. Bulletin of the Seismological Society of America 101, 2369–2387.
Candela, T., Renard, F., Klinger, Y., Mair, K., Schmittbuhl, J., Brodsky, E., 2012. Roughness of fault surfaces over nine decades of length scales. Journal of Geophysical Research 117, B8. http://dx.doi.org/10.1029/2011JB009041.
Chester, J.S., Chester, F.M., Kronenberg, A.K., 2005. Fracture surface energy of the Punchbowl fault, San Andreas system. Nature 437, 133–136.
Cox, B.L., Wang, J.S.Y., 1993. Fractal surfaces: measurement and applications in the earth sciences. Fractals 1, 87–115.
Feder, J., 1988. Fractals. Plenum Press, New-York.
Hadizadeh, J., Johnson, W.K., 2003. Estimating local strain due to comminution in experimental cataclastic textures. Journal of Structural Geology 25, 1973–1979.
Heilbronner, R., Keulen, N., 2006. Grain size and grain shape analysis of fault rocks. Tectonophysics 427, 199–216.
Keller, J., Hall, S., McClay, K., 1997. Shear fracture pattern and microstructural evolution in transpressional fault zones from field and laboratory studies. Journal of Structural Geology 19, 1173–1187.
Kendall, K., 1978. The impossibility of comminuting small particles by compression. Nature 272, 710–711.
Keulen, N., Heilbronner, R., Stünitz, H., Boullier, A.M., Ito, H., 2007. Grain size distributions of fault rocks: a comparison between experimentally and naturally deformed granitoids. Journal of Structural Geology 29, 1282–1300.
King, G., Sammis, C., 1992. The mechanisms of finite brittle strain. Pure and Applied Geophysics 138, 611–640.
Lin, A., 1999. S-C cataclasite in granitic rock. Tectonophysics 304, 257–273.
Lopez, J.M., Schmittbuhl, J., 1998. Anomalous scaling of fracture surfaces. Physical Review E-Statistical, Nonlinear and Soft Matter Physics 57, 6405–6409.
Mair, K., Main, I., Elphick, S., 2000. Sequential growth of deformation bands in the laboratory. Journal of Structural Geology 22, 25–42.
Maloy, K.J., Hansen, A., Hinrichsen, E.L., Roux, S., 1992. Experimental measurements of the roughness of brittle cracks. Physics Review Letters 68, 213–215.
Mandelbrot, B.B., Passoja, D.E., Paullay, A.J., 1984. Fractal character of fracture surfaces of metals. Nature 308, 721–722.
Marone, C., Scholz, C.H., 1989. Particle-size distribution and microstructures within simulated fault gouge. Journal of Structural Geology 11, 799–814.
Menendez, B., Zhu, W., Wong, T.F., 1996. Micromechanics of brittle faulting and cataclastic flow in Berea Sandstone. Journal of Structural Geology 18, 1–16.
Michibayashi, K., 1996. The role of intragranular fracturing on grain size reduction in feldspar during mylonitization. Journal of Structural Geology 18, 17–25.
Monzawa, N., Otsuki, K., 2003. Comminution and fluidization of granular fault materials: implications for fault slip behaviour. Tectonophysics 367, 127–143.
Moore, D., Summers, R., Byerlee, J., 1989. Sliding behaviour and deformation textures of heated illite gouge. Journal of Structural Geology 11, 329–342.
Power, W.L., Durham, W.B., 1997. Topography of natural and artificial fractures in granitic rocks: Implications for studies of rock friction and fluid migration. International Journal of Rock Mechanics and Mining Sciences 34, 979–989.
Power, W.L., Tullis, T.E., Brown, S.R., Boitnott, G.N., Scholz, C.H., 1987. Roughness of natural fault surfaces. Geophysical Research Letters 14, 29–32.
Prasher, C., 1987. Crushing and Grinding Processes Handbook. Wiley, New York.
Renard, F., Voisin, C., Marsan, D., Schmittbuhl, J., 2006. High resolution 3D laser scanner measurements of a strike-slip fault quantify its morphological anisotropy at all scales. Geophysical Research Letters 33, L04305.
Sammis, C., King, G., Biegel, R., 1987. The kinematics of gouge deformation. Pure and Applied Geophysics 125, 777–812.
Sammis, C.G., King, G.C.P., 2007. Mechanical origin of power law scaling in fault zone rock. Geophysical Research Letters 34, L04312.
Sammis, C.G., Osborne, R.H., Anderson, J.L., Banerdt, M., White, P., 1986. Self-similar cataclasis in the formation of fault gouge. Pure and Applied Geophysics 214, 53–78.
Schmittbuhl, J., Gentier, S., Roux, S., 1993. Field measurements of the roughness of fault surfaces. Geophysical Research Letters 20, 639–641.
Schmittbuhl, J., Roux, S., Berthaud, Y., 1994. Development of roughness in crack propagation. Europhysics Letters 28, 585–590.
Schmittbuhl, J., Vilotte, J.P., Roux, S., 1995a. Reliability of self-affine measurements. Physical Review E-Statistical, Nonlinear and Soft Matter Physics 51, 131–147.
Schmittbuhl, J., Schmitt, F., Scholz, C., 1995b. Scaling invariance of crack surfaces. Journal of Geophysical Research 100, 5953–5973.
Steier, K., Schönert, K., 1972. Verformung und Bruchphänomene unter Druckbeanspruchung von sehr kleinen Körnen aus Kalkstein, Quarz und Polystyrol. Dechema Monograph 69, 167–192.
Stünitz, H., Keulen, N., Hirose, T., Heilbronner, R., 2010. Grain size distribution and microstructures of experimentally sheared granitoid gouge at coseismic slip rates: criteria to distinguish seismic and aseismic faults? Journal of Structural Geology 32, 59–69.
Turcotte, D.L., 1992. Fractals and Chaos. In: Geology and Geophysics. Cambridge University Press, New York.
Wang, W., Scholz, C., 1994. Wear processes during frictional sliding of rocks: a theoretical and experimental study. Journal of Geophysical Research 99, 6789–6799.
Wibberley, C., Petit, J.-P., Rives, T., 2000. Micromechanics of shear rupture and the control of normal stress. Journal of Structural Geology 22, 411–427.

Please cite this article in press as: Dyer, H., et al., Scaling properties of fault rocks, Journal of Structural Geology (2012), http://dx.doi.org/10.1016/j.jsg.2012.06.016